

Article

# Microstructure and Mechanical Properties of TaN Thin Films Prepared by Reactive Magnetron Sputtering

Anna Zaman  and Efstathios I. Meletis \*

Department of Materials Science and Engineering, University of Texas at Arlington, Arlington, TX 76019, USA; anna.zaman@mavs.uta.edu

\* Correspondence: meletis@uta.edu; Tel.: +1-817-272-2559

Academic Editor: Grégory Abadias

Received: 7 October 2017; Accepted: 20 November 2017; Published: 23 November 2017

**Abstract:** Reactive magnetron sputtering was used to deposit tantalum nitride (Ta–N) thin films on Si substrate. The effect of varying the N<sub>2</sub> percentage in the N<sub>2</sub>/Ar gas mixture on the Ta–N film characteristics was investigated. Mechanical and tribological properties were studied using nanoindentation and pin-on-disc wear testing. Decreasing the N<sub>2</sub> content in the gas mixture was found to change the film structure from face centered cubic (fcc) TaN (from 25% to 10% N<sub>2</sub>) to highly textured fcc TaN (at 7% N<sub>2</sub>) to a mixture of fcc TaN<sub>1.13</sub> and hexagonal Ta<sub>2</sub>N (at 5% N<sub>2</sub>), and finally to hexagonal Ta<sub>2</sub>N (at 3% N<sub>2</sub>). A high hardness of about 33 GPa was shown by the films containing the hexagonal Ta<sub>2</sub>N phase (5% and 3% N<sub>2</sub>). Decreasing the N<sub>2</sub> content below 7% N<sub>2</sub> was also found to result in microstructural refinement with grain size 5–15 nm. Besides the highest hardness, the film deposited with 3% N<sub>2</sub> content exhibited the highest hardness/modulus ratio (0.13), and elastic recovery (68%), and very low wear rate ( $3.1 \times 10^{-6} \text{ mm}^3 \cdot \text{N}^{-1} \cdot \text{m}^{-1}$ ).

**Keywords:** tantalum nitride; coatings; magnetron sputtering; hardness; microstructure

## 1. Introduction

Materials based on the nitrides of transition metals have attracted considerable interest because of their high hardness, high temperature oxidation resistance and stability, and high wear resistance, which give rise to various applications [1]. Among the different transition metal nitrides (TiN, CrN, HfN, ZrN, etc.), tantalum nitride (Ta–N) is gaining increasing interest due to its excellent chemical and physical properties. Ta–N is a widely used material for producing hard coatings, wear resistant layers, thin film resistors, diffusion barriers in integrated circuits, and mask layers for X-ray lithography [2–10].

Ta–N coatings that are deposited via magnetron sputtering result in a variety of compound solutions, such as body centered cubic (bcc) TaN, hexagonal (hex) TaN, hex Ta<sub>2</sub>N, face centered cubic (fcc) TaN, hex Ta<sub>5</sub>N<sub>6</sub>, tetragonal Ta<sub>4</sub>N<sub>5</sub>, and orthorhombic (orth) Ta<sub>6</sub>N<sub>2.5</sub>, Ta<sub>4</sub>N, Ta<sub>3</sub>N<sub>5</sub> with differing physical, chemical, and mechanical properties [11–18]. The reported values of hardness for various phases of Ta–N thin films, such as hex Ta<sub>2</sub>N, fcc TaN, orth Ta<sub>6</sub>N<sub>2.5</sub> and orth Ta<sub>4</sub>N are 31, 20, 30.8, and 61.8 GPa, respectively [19–25].

Production of Ta–N by reactive sputter deposition while varying the N<sub>2</sub>/(N<sub>2</sub> + Ar) gas ratio is a well-established technique. Previous studies on magnetron sputtered Ta–N films have reported on the change in crystal structure from fcc TaN to hex TaN, and finally to hex Ta<sub>2</sub>N with varying N<sub>2</sub>/(N<sub>2</sub> + Ar) ratio [4,14,26,27]. Most of studies have reported on the hardness of various Ta–N phases, but their microstructure in relation to mechanical properties is scarcely examined. In the present work, Ta–N films were prepared by reactive magnetron sputtering from a Ta target, while systematically varying the N<sub>2</sub>/(N<sub>2</sub> + Ar) gas flow ratio. The main aim of this study was to investigate the effects of

varying N<sub>2</sub> percentage in the gas mixture on the crystal structure, elemental composition, chemical states, microstructure evolution, and eventually mechanical properties of the films.

## 2. Materials and Methods

TaN films were synthesized in a home built reactive magnetron sputtering system [28]. The thin films were deposited on Si (001) wafers using magnetron sputtering of a Ta target (5 cm in diameter and 0.63 cm thick) of 99.9% purity. A low working pressure of 5 mTorr was maintained during deposition for all of the films in a mixture of Ar (99.9% pure) and N<sub>2</sub> (99.9% pure). A constant 50 W DC power was supplied to the Ta target. The substrate holder used was a 10-cm diameter plate, with rotation set to 15 rpm and temperature to 550 °C for all of the depositions. The target to substrate distance was 10 cm, and a negative bias was applied to the substrate to limit the incorporation of oxygen atoms to the coatings [29,30]. The Ta target and the substrate were sputter cleaned with Ar plasma prior to film deposition. Following cleaning, a pure Ta interlayer was deposited for 4 min at 5 mTorr working pressure and 50 W DC applied power. Experiments were carried out at −100 V substrate bias ( $E_B$ ) with a total gas (N<sub>2</sub> + Ar) flow rate of 25 sccm. The N<sub>2</sub> content was varied in the gas mixture from 25% to 3%. A select set of experiments were also carried out at  $E_B = -200$  V while varying the content of N<sub>2</sub> from 7% to 2.5%. Deposition time for all of the films was 1 h.

The crystallographic structure of the films was studied by low angle X-ray diffraction (XRD) in a Bruker D8 Advance diffractometer (Bruker, Billerica, MA, USA) using Cu K $\alpha$  radiation at room temperature. A low incidence angle of 5° was used for the measurements.  $\theta$ –2 $\theta$  scans (not shown) were acquired within a range of 10°–65°, with a scanning speed of 2 s/step to confirm the presence of any texture. The elemental composition and chemical states were investigated using Auger electron spectroscopy (AES) and X-ray photoelectron spectroscopy (XPS), conducted in a Perkin–Elmer Phi 560 ESCA/SAM system (Perkin–Elmer, Waltham, MA, USA) using a non-monochromated Al K $\alpha$  excitation source. The films were sputter cleaned in an Ar<sup>+</sup> environment with 160 eV pass energy for 4 min prior to measurement. Survey scans were conducted in the 0–1200 eV range with 0.1 s dwell time. The Casa XPS software (Version 2.3.14) was used for XPS and AES spectra analysis. The spectra of the films were calibrated using the C 1s peak at 284.5 eV. Relative sensitivity factors for calculation of chemical composition were referred from CASA XPS software. The microstructure of the films was studied by high-resolution transmission electron microscopy (HRTEM). Cross section specimens were prepared by the procedure of mechanical grinding, polishing, dimpling, and Ar ion milling. Selected-area electron diffraction (SAED) patterns and HRTEM images were recorded in a Hitachi H-9500 electron microscope (300 keV, Hitachi, Tokyo, Japan). Film cross section was examined by scanning electron microscopy (SEM) using a Hitachi S-3000N variable pressure microscope (Hitachi, Tokyo, Japan). Film hardness, effective Young's modulus  $E^* = E/(1 - \nu^2)$  (where  $E$  and  $\nu$  are Young's modulus and Poisson's ratio, respectively), and elastic recovery ( $W_e$ ) were determined by a Hysitron Ubi 1 Nanomechanical Test Instrument (Hysitron, Eden Prairie, MN, USA) using a cube corner diamond tip. Depth controlled indentations were performed at less than 10% of the coating thickness to avoid hardness effect of the underlying substrate. The hardness was recorded for 9 indentations (3 × 3 matrix) to get the average value. The thickness, curvature (from which the residual stress was determined using the original Stoney's formula), and surface roughness of the film were measured by a Veeco NT-9100 Optical Surface Profilometer (Veeco Instruments Inc., Plainview, NY, USA). The thickness was determined from the step height between the film and a masked substrate area. A pin-on-disk tribometer (Model TRB, CSM Instruments, Peseux, Switzerland) was used to obtain the coefficient of friction ( $\mu$ ) and the wear rate of the films. A 6 mm alumina ball was used as the pin and it was loaded with 1 N load. The rotation speed was 10 cm/s for a sliding distance of 100 m. All tests were performed at room temperature (21 °C) and normal humidity (~40%). The coefficient of friction was continuously measured during wear testing. The overall wear rate was determined by conducting wear track depth profile analysis using profilometry.

### 3. Results and Discussion

#### 3.1. XRD Analysis

Figure 1 shows the low-angle XRD patterns of the Ta–N films deposited at  $E_B = -100$  V with the  $N_2$  content in the gas mixture varying from 25% to 3%. The XRD spectra of the films with 25%–10%  $N_2$  show diffraction peaks at  $2\theta$  angles of  $35.5^\circ$ ,  $41.3^\circ$ , and  $60.1^\circ$ , which can be identified as the (111), (200), (220) peaks of fcc  $\delta$ -TaN (PDF#49-1283). The 25%  $N_2$  film seems to be textured along (111), and as the  $N_2$  content is decreased from 25% to 10%, the (200) peak gains strength. Decreasing the  $N_2$  content to 7% results in one major peak at  $2\theta$  angle of  $35.3^\circ$  and smaller peaks at  $2\theta$  angles of  $41.07^\circ$  and  $59.79^\circ$ , which can also be identified as the (111), (200), and (220) diffraction peak of the fcc TaN. The 7%  $N_2$  film seems to have a noticeable (111) texture, which was also confirmed by a  $\theta$ – $2\theta$  scan (not shown). All of the above peaks in the 7%  $N_2$  film exhibit a shift to lower angles when compared to (111), (200), (220) diffraction of the fcc TaN crystal structure reported in the powder diffraction file (PDF#49-1283). This is most likely caused by the residual stress in the films, probably due to a defective fcc structure. Further decrease in  $N_2$  to 3% results in diffraction peaks at  $2\theta$  angles of  $33.8^\circ$ ,  $38.4^\circ$ , and  $60.4^\circ$  and can be identified as the (100), (101), (110) planes of hex  $Ta_2N$  (PDF#26-0985). It should be noted that the (002) reflection of the hex- $Ta_2N$  is expected to be present in the shoulder around  $2\theta$  angle of  $36.5^\circ$ .

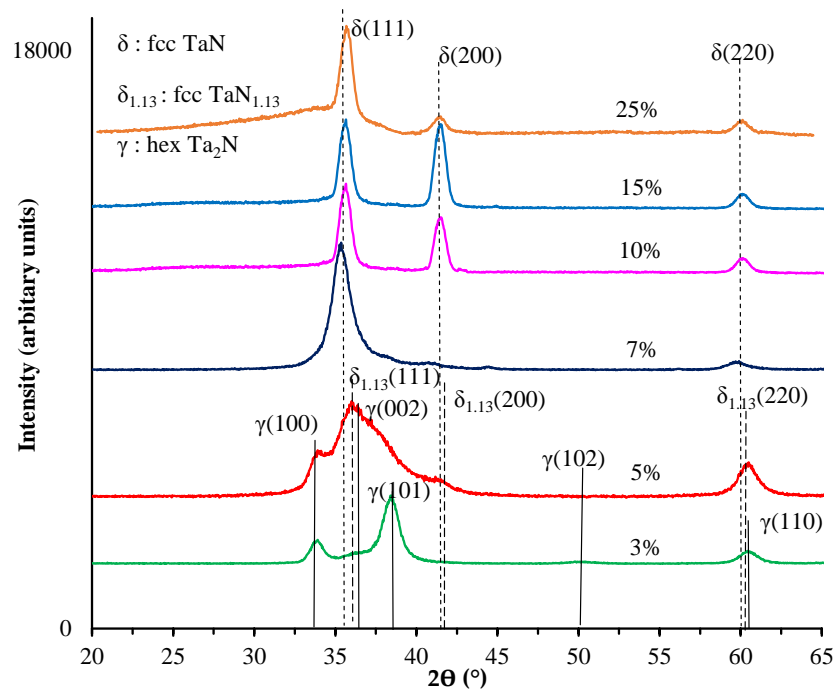


**Figure 1.** Low-angle X-ray diffraction (XRD) of the Ta–N films deposited at  $E_B = -100$  V with  $N_2$  content varying from 25% to 3%.

The XRD pattern of the film deposited with 5%  $N_2$  shows at least two peaks at  $2\theta$  angle of  $33.9^\circ$  and  $60.40^\circ$ , and a broad peak around  $36.02^\circ$ , which in turn is comprised of many peaks. The XRD patterns of the films with 3% and 5%  $N_2$  are shown separately in Figure 2. The peaks at  $33.9^\circ$ ,  $36.02^\circ$ ,  $60.40^\circ$  correspond to (100) of hex  $Ta_2N$ , and (111) and (220) of fcc  $TaN_{1.13}$ . Thus, the XRD spectrum for the film with 5%  $N_2$  shows a mixture of phases and is a transition from a single phase fcc TaN (from 25% to 7%  $N_2$ ) to mainly hex  $Ta_2N$  (3%  $N_2$ ). It should be noted that since the film with 5%  $N_2$  had a mixture of phases, other expected diffractions such as (002), (101) of the hex  $Ta_2N$ , and (200) of the fcc  $TaN_{1.13}$  phase are present in the broad shoulder extending from a  $2\theta$  angle of  $35.83^\circ$  to about  $42^\circ$ , as shown in Figure 2. The hex  $Ta_2N$  phase, which dominates in the 3%  $N_2$  film, was still emerging in the 5% film. The emergence of the hex  $Ta_2N$  phase can also be seen to some extent in the 7%  $N_2$  film, as depicted

by the small shoulder around  $2\theta = 37^\circ\text{--}40^\circ$ , which might correspond to the nanograins of hex  $\text{Ta}_2\text{N}$  phase (possibly beginning to nucleate) as the film crystal structure was undergoing a transition from fcc to hex  $\text{Ta}_2\text{N}$ . The hex  $\text{Ta}_2\text{N}$  phase is well reported in the literature [23,24,31]. It has been reported that TaN has a defective structure and deviations from stoichiometry are frequent [32]. Theoretical analysis suggests that in the Ta–N system,  $\text{Ta}_2\text{N}$  and TaN phases have stable and metastable structures, respectively, and that the energy difference calculated for these two tantalum nitrides is very close [11].

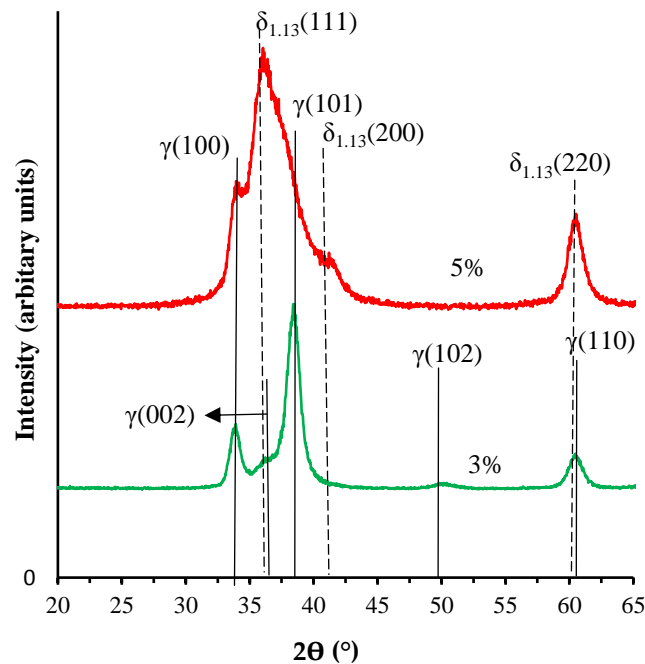


**Figure 2.** Low-angle XRD of the Ta–N films deposited at  $E_B = -100$  V with  $\text{N}_2$  content 5% and 3%.

Figure 3 shows the low-angle XRD of films that are deposited at  $E_B = -200$  V and varying the  $\text{N}_2$  content from 7% to 2.5%. The trend observed for this set of experiments was similar to that shown by the films deposited at similar conditions, but at  $E_B = -100$  V. For the film with 7%  $\text{N}_2$ , the diffractions at  $2\theta$  angle of  $35.15^\circ$ ,  $40.14^\circ$ , and  $59.5^\circ$  can be identified as the (111), (200), and (220) plane of fcc TaN. By comparing the full width half maximum (FWHM), we can say that the fcc (111) peak in this case is broad (FWHM = 0.038 rad) and at slightly lower diffraction angle (larger d-spacing due to compressive residual stresses) than the fcc (111) peak for the film deposited at  $E_B = -100$  V with the same gas ratio of 7% (FWHM = 0.024 rad). The broader peaks indicate refinement in the film microstructure (smaller grain size) and inhomogeneous strains in the lattice that are caused by the consistent energetic bombardment at higher bias. Similar microstructural refinement effects by higher plasma energies have been previously documented [29].

As the  $\text{N}_2$  content is decreased to 5%, diffraction peaks at  $2\theta$  angle of  $33.34^\circ$ ,  $37.91^\circ$ , and  $59.6^\circ$  are observed which can be identified as the (100), (101), and (220) plane of hex  $\text{Ta}_2\text{N}$ . In the case of  $E_B = -200$  V, a transition from fcc TaN to hex  $\text{Ta}_2\text{N}$  was facilitated with no broad transition peak (comprising a mixture of phases), which was observed at  $E_B = -100$  V for the same  $\text{N}_2$  percentage. This indicates that a faster transition is promoted by the higher plasma energy of the system at a higher  $E_B$ . As the  $\text{N}_2$  content is further decreased to 2.5%, hex  $\text{Ta}_2\text{N}$  is still the dominant phase textured along the (101) orientation. The (101) texture is more pronounced when compared to the film that is deposited with almost same content of  $\text{N}_2$  (3%), but at  $E_B = -100$  V. A similar change in crystal structure from fcc TaN to hex  $\text{Ta}_2\text{N}$  with decreasing  $\text{N}_2$  has been reported in the literatures [4,14,26,27].

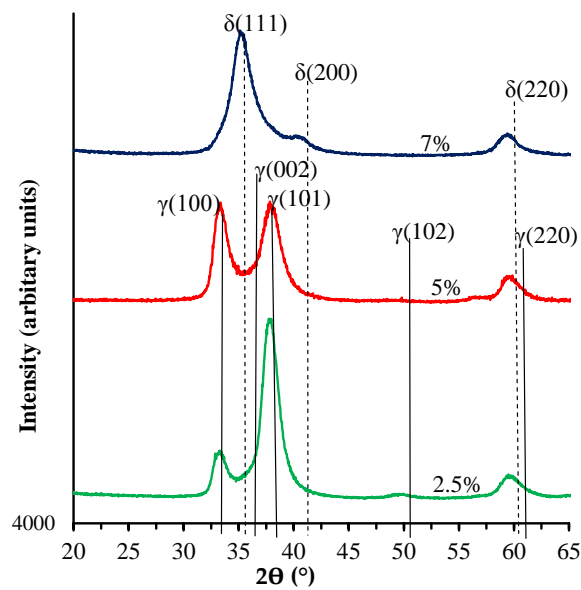


**Figure 3.** Low-angle XRD of the Ta-N films deposited at  $E_B = -200$  V with  $N_2$  content 7%, 5% and 2.5%.

Figure 4 shows the variation in the deposition rate (nm/h) of the films that were deposited at  $E_B$  of  $-100$  V and  $-200$  V. The thickness of the films deposited at  $E_B = -100$  V was around  $500 \pm 30$  nm except for the ones deposited with 7% and 5%  $N_2$ . The 7%  $N_2$  film was textured along fcc (111) and that possibly contributed to the higher deposition rate. The 5%  $N_2$  film comprises mainly of fcc  $TaN_{1.13}$ , but it also contains other phases, resulting in a slight decrease in deposition rate when compared to the 7%  $N_2$  film. However, the trend from 7% to 25%  $N_2$  and 5% to 3% shows a decrease in the deposition rate and can be attributed to the more uniform, non-textured microstructure. The deposition rate of the films deposited at higher bias of  $-200$  V is typically lower due to resputtering. The films deposited with 7% and 2.5%  $N_2$  have a higher deposition rate as compared to the 5% film. The higher deposition rate for these films is due to their texture when compared to the more uniform hex  $Ta_2N$  film. However, the film deposited with 2.5%  $N_2$  at  $E_B = -200$  V has a higher deposition rate than the film deposited with almost same  $N_2$  content (3%) but at  $E_B = -100$  V. Both films have preferred orientation along the (101) plane but analysis of their respective (101) peak heights shows a significant higher texture for the film deposited at  $E_B = -200$  V, resulting in a higher deposition rate.

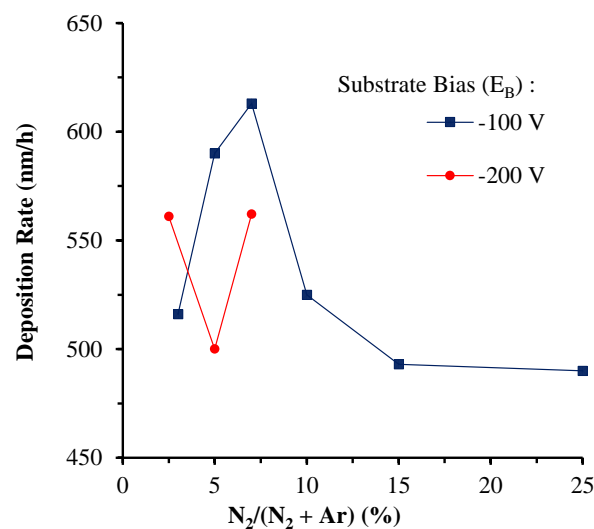


**Figure 4.** Film deposition rate (nm/h) as a function of varying  $N_2$  content with  $E_B = -100$  V and  $-200$  V.

### 3.2. XPS Studies

The composition and chemical state of Ta–N films were examined by AES and XPS, respectively. All of the binding energy values have been corrected for charging effects with reference to the adventitious carbon 1s peak at 284.6 eV. Figure 5 shows the evolution of the elemental composition of the reactively sputtered Ta–N films deposited at  $E_B = -100$  V with  $N_2$  content varying from 25% to 3%. The elemental percentage composition was determined from peak to peak intensity from the differentiated spectrum. A decrease in the N concentration and an increase in the Ta concentration can be observed as the  $N_2$  content in the gas mixture is decreased from 25% to 3%. The Ta/N ratio is approximately 1:1, 1:1.8, 2:1 for 25%–7%, 5%, and 3% flow ratios, respectively. This agrees well with the phases that were identified by XRD.

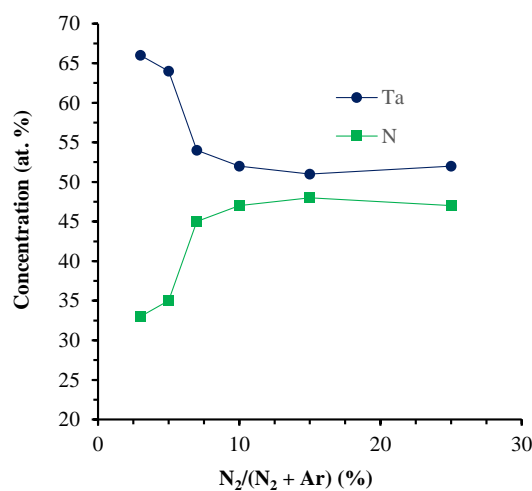


**Figure 5.** Elemental composition of Ta–N films deposited at  $E_B = -100$  V with  $N_2$  content varying from 25% to 3%.

The high-resolution Ta 4f and N 1s spectra for all of the films are shown in Figure 6a,b, respectively. As shown in Figure 6a, the Ta 4f peaks are at higher binding energies when compared to that of metallic Ta (Ta 4f<sub>7/2</sub> ~ 21.7 eV). This peak shift indicates the transition from a metallic (Ta 4f<sub>7/2</sub> ~ 21.7 eV) to a nitride (Ta 4f<sub>7/2</sub> ~ 23 eV) chemical state [26]. We can also observe that as the  $N_2$  content is decreased from 15% to 3%, the binding energy of Ta 4f<sub>7/2</sub> peak is shifted to slightly lower values (23.8, 23.8, 23.7, 23.5 eV and 23.1 eV at 15%, 10%, 7%, 5%, and 3%  $N_2$ , respectively) indicating a change in the chemical state of Ta, possibly due to a change in binding state from TaN to Ta<sub>2</sub>N, as observed by XRD (Figure 1). As is seen, the Ta 4f peak for 7% and 5% film is broad. This depicts the presence of two binding states, possibly TaN and Ta<sub>2</sub>N, as these films were undergoing a transition from fcc TaN to hex Ta<sub>2</sub>N. Actually, the presence of nucleating hex Ta<sub>2</sub>N nanograins was seen in the XRD spectrum of the 7% film. At 25%  $N_2$ , the intensity of the Ta 4f peak decreases and the peak becomes broader, while the binding energy of Ta 4f<sub>7/2</sub> shifts to 23.2 eV. This indicates the presence of some other chemical states or defects at the surface, which resulted in the lower binding energy of Ta 4f peak. A similar broad peak with a decreased intensity of the Ta 4f peak at a higher  $N_2$  fraction was also reported by Arshi et al. [27]. As shown in Figure 6b, the N 1s peak is ~397 eV and this corresponds to binding energy of nitrogen in a metal nitride state, although the Ta 4p<sub>3/2</sub> peak at 403.5 eV is almost constant. It can also be seen that there is a decrease in the intensity of the N 1s peak with decreasing  $N_2$  content, which is consistent with the compositional analysis (Figure 5). For the 25% film, the N 1s peak showed a slight shift to a lower binding energy, similar to the shift in Ta 4f peak, possibly due to excess N in the film. In the case of lower  $N_2$  content films, (7%, 5%, and 3%), the N 1s peak shows some broadness. This broad peak corresponds to two binding energies, 398.1 eV and 397.2 eV, and can be attributed to the presence of two phases.

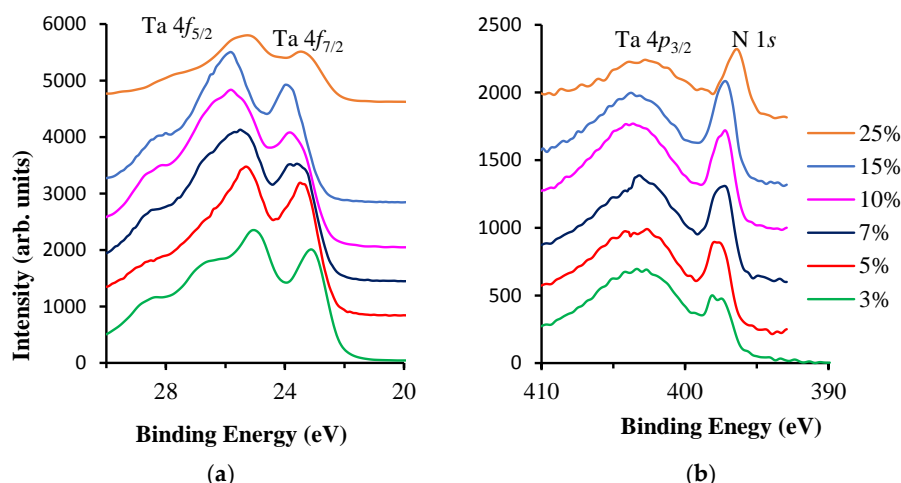


**Figure 6.** High resolution X-ray photoelectron spectroscopy (XPS) (a) Ta 4f and (b) N 1s spectra for films deposited with N<sub>2</sub> content varying from 25% to 3%.

Figure 7a,b shows the deconvoluted peaks for films deposited with 3% and 25% N<sub>2</sub>, respectively, where the solid black line represents experimental values and dashed lines represent the deconvolution. The spectra for these films are composed of two sets of Ta 4f doublets. When considering the split energy by spin orbit coupling of 4f<sub>7/2</sub> and 4f<sub>5/2</sub> in Ta 4f as 1.9 eV, the high energy side doublet for all of the films shows the binding energy of Ta 4f<sub>7/2</sub> to be 26.2 eV and of Ta 4f<sub>5/2</sub> close to 28.2 eV, which is close to the chemical state of Ta in Ta<sub>2</sub>O<sub>5</sub> (Ta 4f<sub>7/2</sub> = 26.2 eV) [26,33]. Regarding the low energy side doublet, the binding energy of Ta 4f<sub>7/2</sub> is around 23.1 eV and of Ta 4f<sub>5/2</sub> close to 25.1 eV, which correspond to binding states of Ta in Ta–N system (4f<sub>7/2</sub> = 23 eV and 4f<sub>5/2</sub> = 25 eV) [34]. The fraction of Ta<sub>2</sub>O<sub>5</sub> binding state is higher for the 3% N<sub>2</sub> as compared to 25% N<sub>2</sub> film, which is evident from the intensity of the high-energy side shoulder in the Ta 4f spectra, which increases with a decreasing N<sub>2</sub> content in the gas mixture. It looks like the incorporation of residual oxygen in crystalline Ta–N is reduced as the N<sub>2</sub> content increases. A similar effect has been reported by Chang et al. [26]. Figure 8a,b shows the deconvolution of the N 1s peak, including the Ta 4p<sub>3/2</sub> for the 5% and 25% N<sub>2</sub> film, respectively. As seen in the 25% N<sub>2</sub> film, the N 1s peak is around 397 eV, whereas the 5% N<sub>2</sub> peak can be deconvoluted into two peaks with binding energies, 397.2 eV and 398.1 eV. The presence of these two peaks in the low N<sub>2</sub> content films is consistent with the TaN and Ta<sub>2</sub>N phases detected by XRD. Thus, the XPS findings are in agreement with XRD data adding additional insight to the gradual nucleation and growth of the Ta<sub>2</sub>N phase as the N<sub>2</sub> content decreases.

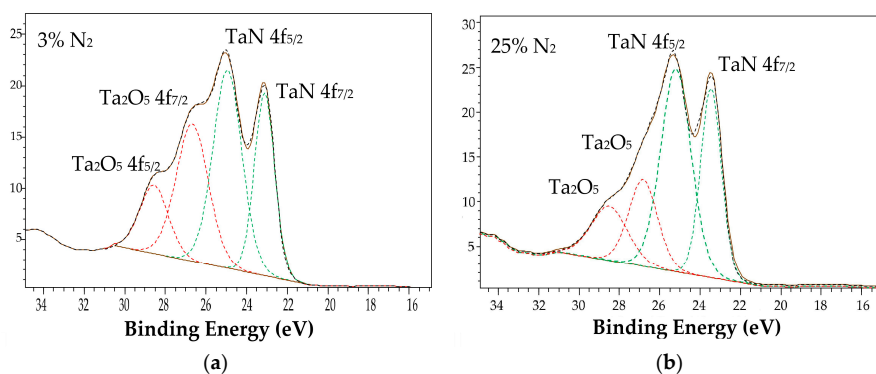


**Figure 7.** Deconvoluted XPS spectra of Ta 4f core levels for Ta–N films deposited with (a) 3% and (b) 25% N<sub>2</sub>.

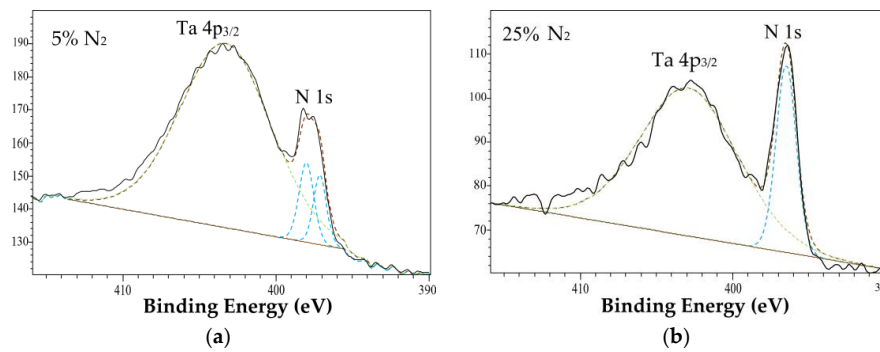


**Figure 8.** Deconvoluted XPS spectra of N 1s core levels for Ta–N films deposited with (a) 5% and (b) 25% N<sub>2</sub>.

### 3.3. Microstructural Investigation

In order to understand the effect of varying N<sub>2</sub> content in the gas mixture on the microstructure of the Ta–N films, three films were selected to be analyzed using TEM. These were the films deposited at  $E_B = -100$  V with 7%, 5%, and 3% N<sub>2</sub>.

#### 3.3.1. Ta–N Film Deposited with 7% N<sub>2</sub>

Figure 9a is a cross section bright field TEM image of the bulk structure of the film deposited with 7% N<sub>2</sub>, showing signs of columnar morphology along the growth direction. Figure 9b is a cross section bright field TEM image showing the interface between the Si substrate and the Ta–N film. The film shows a sharp interface with the substrate via a Ta adhesion layer, which is ~60 nm thick with a seamless transition to the TaN film. A similar smooth transition was observed for the films with 5% and 3% N<sub>2</sub>. The SAED pattern that is shown as an inset in Figure 9b was taken from an area in the film (away from the film/Si interface) and shows a single diffraction ring with lattice spacing 2.5 Å. This can be identified as the (111) plane of fcc TaN. The SAED pattern agrees well with the XRD pattern for this film where a single peak was observed corresponding to fcc TaN, as shown in Figure 1. Figure 9c is a HRTEM image from a cross section of this film that depicts the presence of 5–15 nm size grains (shown by circles) separated by amorphous boundaries (shown by dotted lines).

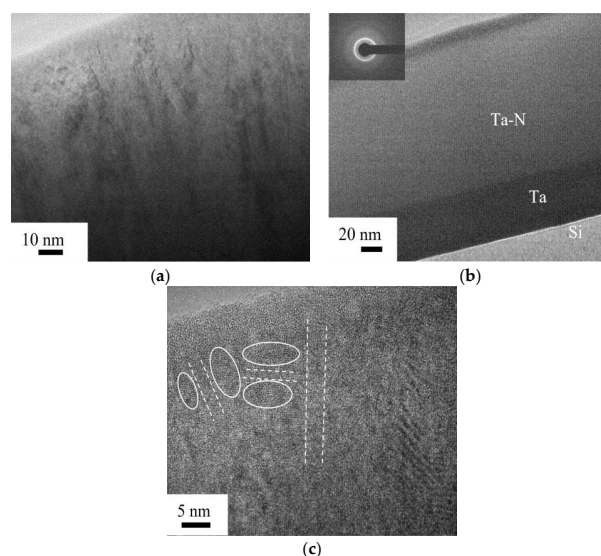


**Figure 9.** (a) TEM image and (b) TEM image of film/Si interface (inset is the selected-area electron diffraction (SAED) pattern); (c) high resolution transmission electron microscopy (HRTEM) image from a cross section of the film sputtered with 7% N<sub>2</sub>.

### 3.3.2. Ta–N Film Deposited with 5% N<sub>2</sub>

Figure 10a is a cross section bright field TEM image of the film deposited with 5% N<sub>2</sub> showing very fine needle like structures and some rounded structures, indicating the presence of more than one phase. This agrees well with the XRD pattern (Figure 2), which clearly showed a mixture of phases for this film. Figure 10b is a typical SAED pattern taken from an area away from the film/Si interface showing several diffractions. The first diffraction ring (1) has a lattice spacing of 2.63 Å and can be identified as the (100) plane of hex Ta<sub>2</sub>N. The diffraction spots (2) at the outer diameter of the first ring (1), have a lattice spacing of 2.14 Å and can be identified as the (200) plane of fcc TaN<sub>1.13</sub>. The expected (111) diffraction of fcc TaN<sub>1.13</sub> and (002), (101) of hex Ta<sub>2</sub>N with lattice spacing 2.49 Å, 2.45 Å, and 2.32 Å, respectively, are present in this diffused diffraction arc but cannot be differentiated. This agrees with the broad transition peak that was observed in the XRD pattern for this film (Figure 2). The diffraction ring (3) with lattice spacing 1.52 Å can be assigned mainly to the (220) plane of fcc TaN<sub>1.13</sub> (and also to (110) of hex Ta<sub>2</sub>N).

The diffraction ring (4) with lattice spacing 1.29 Å can be assigned to the (220) plane of hex TaN. It should be noted that the (220) peak for hex TaN was not visible in the XRD as it shows diffraction at 2θ angle of 72.9°, which is beyond 65° of the diffraction pattern. Figure 10c is a cross section HRTEM image of the film clearly showing randomly oriented elongated and rounded grains depicting more than one morphology. Nanograins with a typical size of 2–5 nm with no visible amorphous boundaries between grains can be observed.

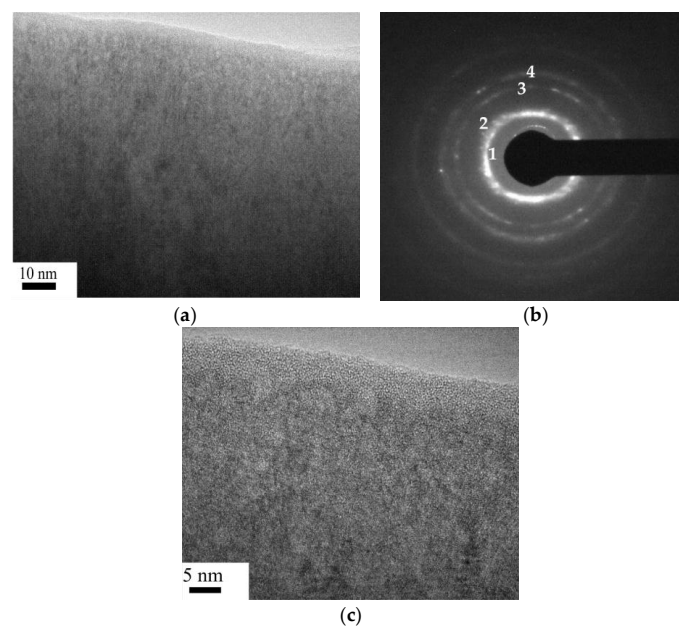
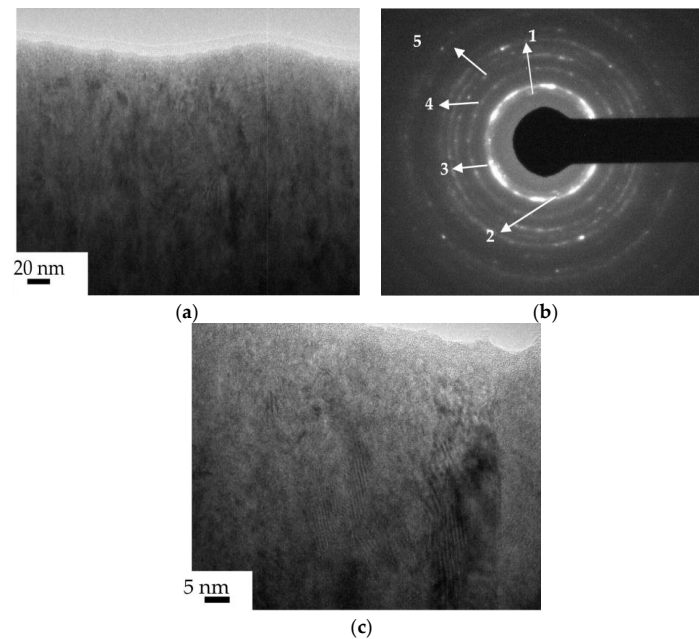


**Figure 10.** (a) TEM image; (b) SAED pattern; and (c) HRTEM image from a cross section TEM foil of a Ta–N film deposited with 5% N<sub>2</sub>.

### 3.3.3. Ta–N Film Deposited with 3% N<sub>2</sub>

Figure 11a is a cross section bright field TEM image of the film deposited with 3% N<sub>2</sub> showing the presence of nano-needle like structures. The nano–needles have a lateral size of ~5–10 nm and a length of ~20–30 nm. Figure 11b is a typical SAED pattern that is taken from an area in the film (away from the film/Si interface) showing several diffractions. The four diffraction rings (1), (3), (4), and (5) with lattice spacing 2.63 Å, 2.30 Å, 1.78 Å, and 1.5 Å, respectively, can be identified as the (100), (101), (102), (110) plane of hex Ta<sub>2</sub>N. The diffraction ring (2) with lattice spacing 2.49 Å corresponds to the (111) plane of fcc TaN<sub>1.13</sub> phase. The presence of this phase could also be seen in the shoulder around 2θ angle of 36° in the XRD pattern for this film (Figure 2). Also, as is evident from the SAED pattern,

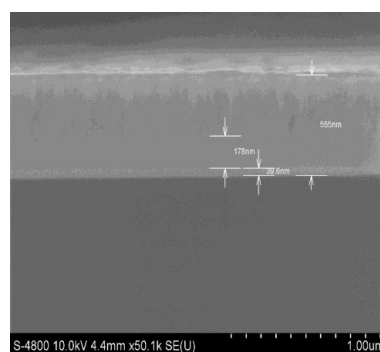
the diffraction arcs are discontinuous, indicating the ordering of the columnar grains (in this case nano-needles) in the in-plane direction. This is in addition to the texture in the films developed along the growth direction as detected by XRD, which showed the (101) plane of the hex  $\text{Ta}_2\text{N}$ , d-spacing 2.30 Å as the high intensity peak. The (002) and (102) diffractions of hex  $\text{Ta}_2\text{N}$  were absent in the XRD pattern for this sample. These observations show that both random and textured regions exist in the film. Figure 11c is a HRTEM image taken from an area away from the film/substrate interface. The grain size varies from 5 to 10 nm. Most grains are interconnected with their adjacent grains directly without the presence of amorphous boundaries. Very few amorphous boundaries were formed between the grains.



**Figure 11.** (a) Bright field TEM image; (b) SAED pattern; and (c) HRTEM image from a cross section of a Ta–N film deposited with 3%  $\text{N}_2$ .

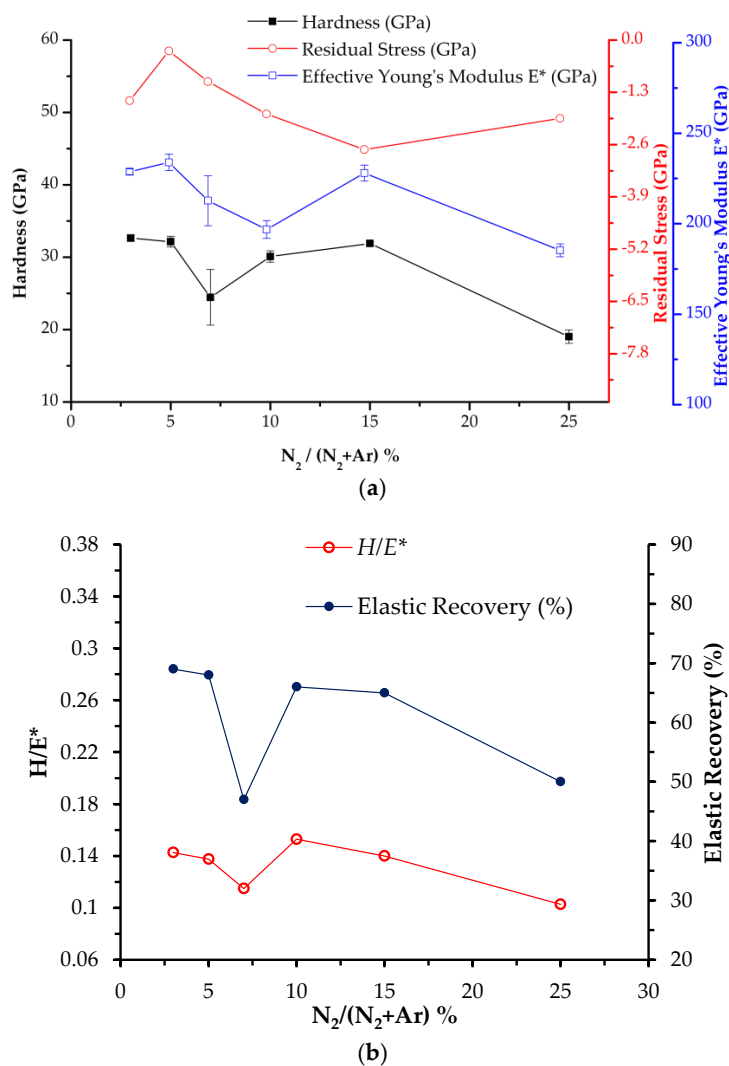
#### 3.4. Film Morphology, Mechanical and Tribological Properties

Figure 12 shows the cross section morphology of the Ta–N film deposited with 3%  $\text{N}_2$ . The cross section shows a dense film with a sharp interface between the Ta adhesion layer (~40 nm) and the substrate, as well as a smooth transition from the adhesion layer to the TaN film. It is also evident that initially a smooth, featureless Ta–N film grows (~180 nm) from the Ta interlayer, and subsequently, the film develops a nanocolumnar structure. The surface roughness was measured by optical profilometry and was around 10 nm for all films.



**Figure 12.** Scanning electron micrograph from a cross-section of the Ta–N film deposited with 3%  $\text{N}_2$ .

Nanoindentation experiments were conducted to study the effect of the varying  $N_2$  content in the gas mixture on the mechanical properties of the films. Figure 13a shows the variation in hardness, effective Young's modulus, and residual stress as a function of the  $N_2$  content of films deposited at  $E_B = -100$  V. As the  $N_2$  content is decreased from 25% to 3%, there is an increase in hardness from  $\sim 20$  to  $\sim 33$  GPa. However, the 7%  $N_2$  film shows a lower hardness of  $\sim 24$  GPa. This decrease in hardness is possibly due to the texture that is developed in the film depicting a preferred fcc (111) orientation (Figure 1), as compared to the 10% and 15%  $N_2$  film, which have a more uniform non-textured fcc crystal structure. Hardness value of  $\sim 20$  GPa for fcc TaN has been previously reported in the literature [25]. As can be seen, the 25%  $N_2$  film also showed preferred fcc (111) orientation and displayed a hardness of  $\sim 20$  GPa. The 7%  $N_2$  film shows comparable hardness but with larger scatter than the 25%  $N_2$  film. This can be attributed to the nucleation of the higher hardness hex  $Ta_2N$  nanograins in the 7%  $N_2$  film (Figure 1). Decreasing the  $N_2$  content to 5% and 3% results in higher hardness of around 33 GPa due to change in crystal structure from dominant fcc TaN (25% to 7%  $N_2$ ) to a mixture of fcc  $TaN_{1.13}$  and hex  $Ta_2N$  (for 5%  $N_2$ ), and finally to hex  $Ta_2N$  (for 3%  $N_2$ ). The variation in effective Young's modulus shows a similar trend like the variation in hardness and increases from  $\sim 185$  GPa to  $\sim 230$  GPa as we decrease  $N_2$  content from 25% to 3%.

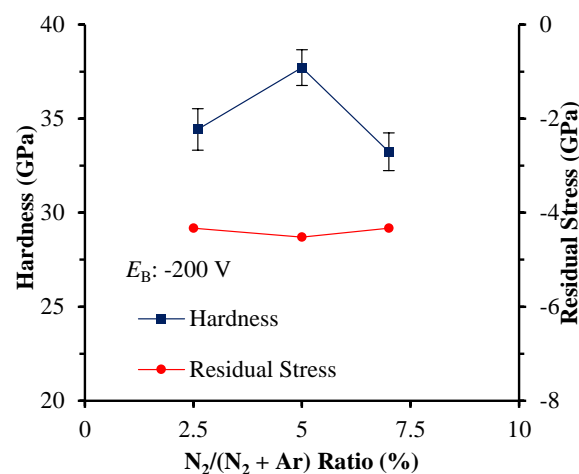


**Figure 13.** (a) Variation in hardness, effective modulus and residual stress and (b)  $H/E^*$  ratio and Elastic Recovery,  $W_e$  (%) of films sputtered at  $E_B = -100$  V with  $N_2$  content varying from 25% to 3%.

The low residual stress observed for the 5% N<sub>2</sub> film when compared to the rest of the films is more likely due to the formation of a mixture of phases in this film. The 3% film exhibited a good combination of hardness (~33 GPa) accompanied with a relatively low residual stress (~−1.5 GPa). Nano-needle like structures that were observed for this film play a critical role in the enhancement of film hardness (Figure 11). Nano-needle like structures usually have a single crystal structure and exhibit strong preferred crystallographic orientation. The hardness enhancement due to the presence of nano-needle like structures is very similar to the enhanced enhancement due to nano-columnar morphology where dislocation formation is unlikely when the size of nanocolumns is ~5–10 nm. Even if dislocations did nucleate during indentation, dislocation motion would be impeded due to the transition from one crystallographic orientation to another [35–37].

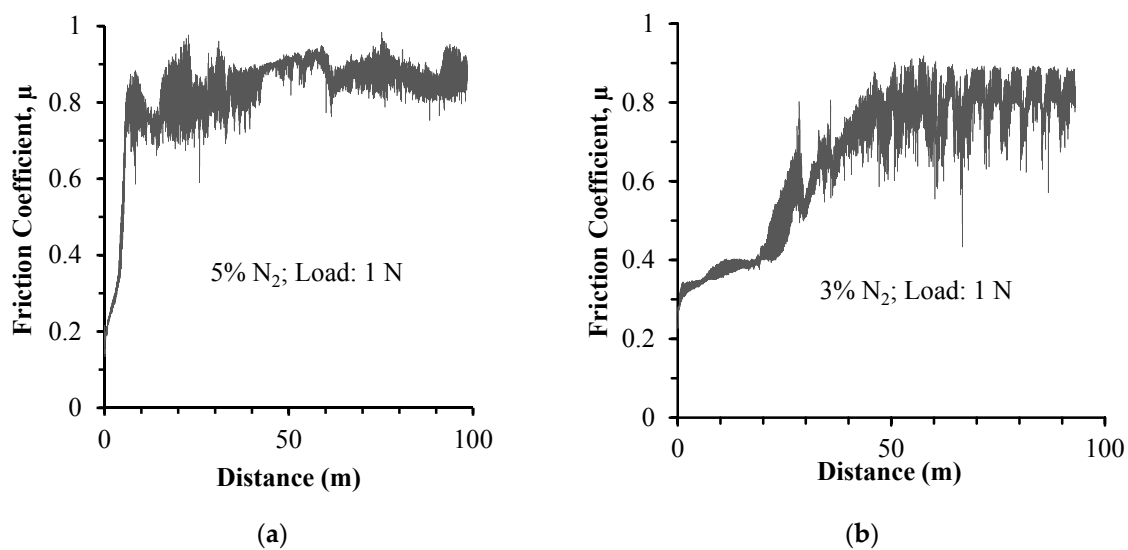
Figure 13b presents the variation of  $H/E^*$  ratio and elastic recovery  $W_e$  (%) of the films as a function of the N<sub>2</sub> content. It has been reported previously that hard coatings with enhanced resistance to cracking are characterized by a high ratio  $H/E^* \geq 0.1$  and high elastic recovery  $W_e > 60\%$  [36,38]. It is interesting to note that all of the present Ta–N films exhibited a high  $H/E^* \geq 0.1$ . In addition, high elastic recovery of >65%, was exhibited by most films except for the film that was deposited with 7% and 25% N<sub>2</sub> content. This reduction in elastic recovery can be possibly attributed to their textured crystal structure. Overall, it seems that films deposited with low N<sub>2</sub> content (5% and 3%) display desirable mechanical properties, i.e., high resistance to deformation, resistance to cracking and low residual stresses.

Figure 14 shows the variation of hardness and residual stress of films deposited at  $E_B = -200$  V and varying the N<sub>2</sub> content. Decreasing the N<sub>2</sub> content from 7% to 5% results in an increase in hardness from ~33 to ~37 GPa. This can be attributed to the crystal structure change from fcc TaN to hex Ta<sub>2</sub>N. A further decrease in N<sub>2</sub> content from 5% to 2.5% results in a decrease of hardness from ~37 to ~34 GPa. The crystal structure that is present in both the latter films is hex Ta<sub>2</sub>N, however, the 2.5% N<sub>2</sub> film shows significant texture along the (101) plane (Figure 3). This more than likely can account for the slight decrease in the hardness. All three of the films were accompanied by relatively high residual stress of about −4 GPa. The higher energy delivered to these films by Ar<sup>+</sup> (due to higher kinetic energy at higher  $E_B$ ) and can account for their higher residual stresses when compared to films that are deposited at lower bias voltage, Figure 13a.



**Figure 14.** Variation in hardness and residual stress of films deposited with  $E_B = -200$  V and N<sub>2</sub> content varying from 7% to 2.5%.

Pin on disc experiments were performed on Ta–N films which were deposited at  $E_B = -100$  V, with 5% and 3% N<sub>2</sub> content and exhibited high  $H/E^*$  ratio (0.13) and  $W_e$  (68%). The coefficient of friction was found to vary between  $\mu = 0.7$ – $0.9$ , with the film deposited with 3% N<sub>2</sub> exhibiting slightly lower values, Figure 15a,b.



**Figure 15.** Coefficient of friction ( $\mu$ ) for films deposited with (a) 5% and (b) 3%  $N_2$ .

Figure 16 presents the two-dimensional wear track profiles for the aforementioned films. As can be seen, the wear track of the 5%  $N_2$  film is much wider ( $\sim 220 \mu\text{m}$ ) when compared to 3%  $N_2$  film ( $\sim 40 \mu\text{m}$ ). Similarly, the 3%  $N_2$  film showed a slightly lower wear track depth ( $\sim 32 \mu\text{m}$ ) as compared to 5%  $N_2$  film ( $\sim 34 \mu\text{m}$ ). Overall, the 3%  $N_2$  film exhibited almost an order of magnitude lower wear rate ( $3.1 \times 10^{-6} \text{ mm}^3 \cdot \text{N}^{-1} \cdot \text{m}^{-1}$ ) when compared to the 5%  $N_2$  film ( $2.8 \times 10^{-5} \text{ mm}^3 \cdot \text{N}^{-1} \cdot \text{m}^{-1}$ ).

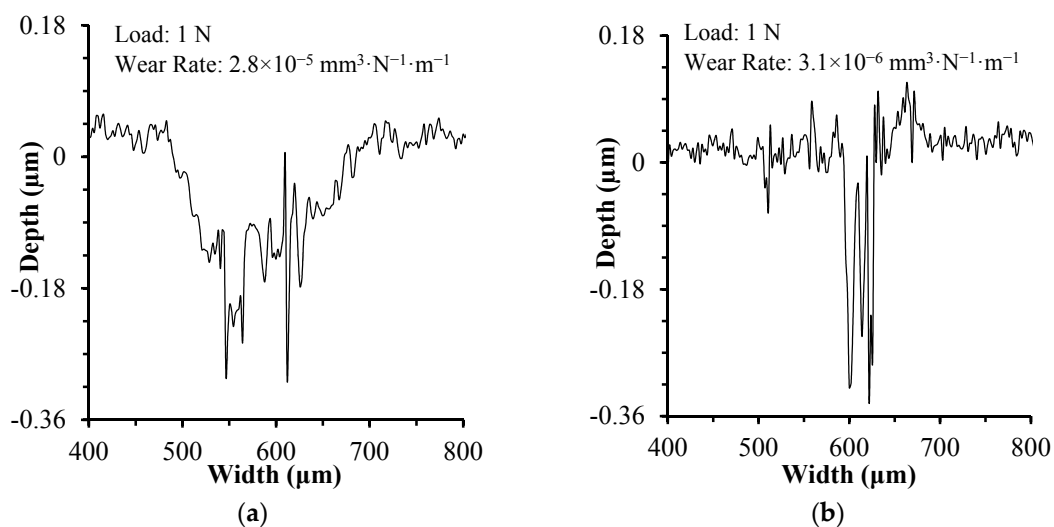


**Figure 16.** Two dimensional profiles of wear tracks for films deposited with (a) 5% and (b) 3%  $N_2$ .

When considering the microstructure of these two films, the higher wear rate of the 5%  $N_2$  film is attributed to the presence of both fcc TaN and hex  $Ta_2N$  phases, which can produce a three body wear at the contact resulting in the faster wear rate of the 5%  $N_2$  film. On the contrary, the 3%  $N_2$  film has a uniform microstructure that is composed of a hard hex  $Ta_2N$  phase present as fine nano-needles and a grain size of 5–10 nm, Figure 11. The reported values for wear rate for magnetron sputtered Ta–N coatings are between  $1.4 \times 10^{-5}$  and  $6.2 \times 10^{-5} \text{ mm}^3 \cdot \text{N}^{-1} \cdot \text{m}^{-1}$  [23]. The crystal structure for these coatings was a mixture of bcc Ta and hex  $Ta_2N$  with hardness  $\sim 30 \text{ GPa}$  and high residual stress of  $\sim 5 \text{ GPa}$ . Another group reports wear rate of  $\sim 2.876 \times 10^{-5} \text{ mm}^3 \cdot \text{N}^{-1} \cdot \text{m}^{-1}$  for Ta–N films (with fcc TaN crystal structure), with  $\mu = 0.3$ , and  $H/E^*$  ratio of 0.029 [39]. When compared to the

aforementioned wear rate in the literature, the 3% N<sub>2</sub> film exhibited a significantly low wear rate, high  $H/E^*$  ratio (0.13), and high elastic recovery (~65%), and can serve as a potential coating material for tribological applications.

#### 4. Conclusions

Ta–N films were deposited on Si substrate at 550 °C using reactive magnetron sputtering by varying the nitrogen content in the N<sub>2</sub>/Ar gas mixture. Dense, smooth nanocrystalline Ta–N films were produced with sharp interface with the substrate and low surface roughness. The grown films were found to have fcc TaN phase for 25%–7% N<sub>2</sub>, a mixture of fcc TaN<sub>1.13</sub> and hexagonal Ta<sub>2</sub>N for 5% N<sub>2</sub>, and only hexagonal Ta<sub>2</sub>N for 3% N<sub>2</sub> in the sputtering gas. Besides promoting the formation of the hexagonal Ta<sub>2</sub>N phase, decreasing the N<sub>2</sub> content in the gas mixture below 7% N<sub>2</sub> was found to result in a refining of the microstructure with grain size from 5 to 15 nm. The films deposited with 5% and 3% N<sub>2</sub> content exhibited the highest hardness (33 GPa),  $H/E^*$  ratio (0.13) and  $W_e$  (68%). In particular, the film deposited with 3% N<sub>2</sub> exhibited very low wear rate ( $3.1 \times 10^{-6} \text{ mm}^3 \cdot \text{N}^{-1} \cdot \text{m}^{-1}$ ) and seems to be a potential material for tribological applications.

**Acknowledgments:** This work was carried out in the SaNEL (Surface and Nano-Engineering Laboratory) and CCMB (Characterization Center for Materials and Biology) facilities in the Materials Science and Engineering Department at the University of Texas at Arlington. The authors would like to thank Mingui Zhang and Yi Shen for helping with the nanoindentation and TEM analysis. This work was supported in part by the U.S. National Science Foundation under Award No. NSF/CMMI DMREF-1335502.

**Author Contributions:** Both authors participated and discussed this work and contributed to the submitted and published manuscript.

**Conflicts of Interest:** The authors declare no conflict of interest.

#### References

- Hultman, L. Thermal stability of nitride thin films. *Vacuum* **2000**, *57*, 1–30. [[CrossRef](#)]
- Sundgren, J.E.; Johansson, B.O.; Rockett, A.; Barnett, S.A.; Greene, J.E. TiN: A Review of the Present Understanding of the Atomic Electronic Structure and Recent Results on the Growth and Physical Properties of Epitaxial TiN<sub>x</sub> (0.6 < x < 1.2) Layers. In *Physics and Chemistry of Protective Coatings: Universal City, CA, 1985*; Greene, J.E., Sproul, W.D., Thornton, J.A., Eds.; AIP Conference Proceedings Series 149; American Institute of Physics: New York, NY, USA, 1986; p. 95.
- Liu, X.; Ma, G.; Sun, G.; Duan, Y.; Liu, S. Effect of deposition and annealing temperature on mechanical properties of TaN film. *Appl. Surf. Sci.* **2011**, *258*, 1033–1037. [[CrossRef](#)]
- Riekkinen, T.; Molarius, J.; Laurila, T.; Nurmela, A.; Suni, I.; Kivilahti, J.K. Reactive sputter deposition and properties of Ta<sub>x</sub>N thin films. *Microelectron. Eng.* **2002**, *64*, 289–297. [[CrossRef](#)]
- Lin, J.C.; Lee, C. Growth of Tantalum Nitride Films on Si by Radio Frequency Reactive Sputtering of Ta in N<sub>2</sub>/Ar Gas Mixtures: Effect of Bias. *J. Electrochem. Soc.* **2000**, *147*, 713–718. [[CrossRef](#)]
- Hieber, K. Structural and electrical properties of Ta and Ta nitrides deposited by chemical vapour deposition. *Thin Solid Films* **1974**, *24*, 157–164. [[CrossRef](#)]
- Bhushan, B.; Gupta, B.K. *Handbook of Tribology: Materials, Coatings, and Surface Treatments*; McGraw-Hill Book Company: New York, NY, USA, 1991; p. 1168.
- Kim, S.K.; Cha, B.C. Deposition of tantalum nitride thin films by D.C. magnetron sputtering. *Thin Solid Films* **2005**, *475*, 202–207. [[CrossRef](#)]
- Schauer, A.; Roschy, M.R.F. sputtered β-tantalum and bcc tantalum films. *Thin Solid Films* **1972**, *12*, 313–317. [[CrossRef](#)]
- Sun, X.; Kolawa, E.; Chen, J.; Reid, J.; Nicolet, M.A. Properties of reactively sputter-deposited TaN thin films. *Thin Solid Films* **1993**, *236*, 347–351. [[CrossRef](#)]
- Stampfl, C.; Freeman, A.J. Stable and metastable structures of the multiphase tantalum nitride system. *Phys. Rev. B* **2005**, *71*, 024111. [[CrossRef](#)]

12. Stavrev, M.; Fischer, D.; Wenzel, C.; Dreschen, K.; Mattern, N. Crystallographic and morphological characterization of reactively sputtered Ta, TaN and TaNO thin films. *Thin Solid Films* **1997**, *307*, 79–88. [[CrossRef](#)]
13. Nakao, S.; Numata, M.; Ohmi, T. Thin and low-resistivity tantalum nitride diffusion barrier and giant-grain copper interconnects for advanced ULSI metallization. *J. Appl. Phys.* **1999**, *38*, 2401–2405. [[CrossRef](#)]
14. Nie, H.; Xu, S.; You, L.; Yang, Z.; Wang, S.; Ong, C. Structural and electrical properties of tantalum nitride thin films fabricated by using reactive radio-frequency magnetron sputtering. *Appl. Phys. A* **2001**, *73*, 229–236. [[CrossRef](#)]
15. Lee, W.H.; Lin, J.C.; Lee, C. Characterization of tantalum nitride films deposited by reactive sputtering of Ta in N<sub>2</sub>/Ar gas mixtures. *Mater. Chem. Phys.* **2001**, *68*, 266–271. [[CrossRef](#)]
16. Gerstenberg, D.; Calbick, C.J. Effects of nitrogen, methane, and oxygen on structure and electrical properties of thin tantalum films. *J. Appl. Phys.* **1964**, *35*, 402. [[CrossRef](#)]
17. Terao, N. Structure of tantalum nitrides. *Jpn. J. Appl. Phys.* **1971**, *10*, 248. [[CrossRef](#)]
18. Leng, Y.X.; Sun, H.; Yang, P.; Chen, J.Y.; Wang, J.; Wan, G.J.; Huang, N.; Tian, X.B.; Wang, L.P.; Chu, P.K. Biomedical properties of tantalum nitride films synthesized by reactive magnetron sputtering. *Thin Solid Films* **2001**, *398–399*, 471–475. [[CrossRef](#)]
19. Valletti, K.; Subrahmanyam, A.; Joshi, S.V.; Phani, A.R.; Passacantando, M.; Santucci, S. Studies on phase dependent mechanical properties of dc magnetron sputtered TaN thin films: Evaluation of super hardness in orthorhombic Ta<sub>4</sub>N phase. *J. Phys. D Appl. Phys.* **2008**, *41*, 045409. [[CrossRef](#)]
20. Mori, H.; Imahori, J.; Oku, T.; Murakami, M. Diffusion barriers between Si and Cu. *AIP Conf. Proce.* **1998**, *418*, 475.
21. Stavrev, M.; Wenzel, C.; Moller, A.; Drescher, K. Sputtering of tantalum-based diffusion barriers in SiCu metallization: Effects of gas pressure and composition. *Appl. Surf. Sci.* **1995**, *91*, 257–262. [[CrossRef](#)]
22. Lee, Y.K.; Khin, L.M.; Kim, J.; Kangsoo, L. Study of diffusion barrier properties of ionized metal plasma (IMP) deposited TaN between Cu and SiO<sub>2</sub>. *Mater. Sci. Semicond. Process.* **2000**, *3*, 179–184. [[CrossRef](#)]
23. Westergard, R.; Bromark, M.; Larsson, M.; Hedenqvist, P.; Hogmark, S. Mechanical and tribological characterization of DC magnetron sputtered tantalum nitride thin films. *Surf. Coat. Technol.* **1997**, *97*, 779–784. [[CrossRef](#)]
24. Lee, G.R.; Kim, H.; Choi, H.S.; Lee, J.J. Superhard tantalum-nitride films formed by inductively coupled plasma-assisted sputtering. *Surf. Coat. Technol.* **2007**, *201*, 5207–5210. [[CrossRef](#)]
25. Bernoulli, D.; Müller, U.; Schwarzenberger, M.; Hauert, R.; Spolenak, R. Magnetron sputter deposited tantalum and tantalum nitride thin films: An analysis of phase, hardness and composition. *Thin Solid Films* **2013**, *548*, 157–161. [[CrossRef](#)]
26. Chang, C.C.; Jeng, J.S.; Chen, J.S. Microstructural and electrical characteristics of reactively sputtered Ta–N thin films. *Thin Solid Films* **2002**, *413*, 46–51. [[CrossRef](#)]
27. Arshi, N.; Lu, J.; Lee, C.G.; Koo, B.H.; Ahmed, F. Effects of nitrogen content on the phase and resistivity of TaN thin films deposited by electron beam evaporation. *J. Miner. Met. Mater. Soc.* **2014**, *66*, 1893–1899. [[CrossRef](#)]
28. Zaman, A. Characterization of Tantalum Nitride Thin Films Synthesized by Magnetron Sputtering. Master's Thesis, University of Texas at Arlington, Arlington, TX, USA, May 2014.
29. Adjaottor, A.A.; Ma, E.; Meletis, E.I. On the mechanism of intensified plasma-assisted processing. *Surf. Coat. Technol.* **1997**, *89*, 197–203. [[CrossRef](#)]
30. Veprek, S.; Karvankova, P.; Veprek-Heijman, M.G.J. Possible role of oxygen impurities in degradation of nc-TiN/a-Si<sub>3</sub>N<sub>4</sub> nanocomposites. *J. Vac. Sci. Technol. B* **2005**, *23*, L17–L21. [[CrossRef](#)]
31. Shin, C.-S.; Kim, Y.-W.; Gall, D.; Greene, J.E.; Petrov, I. Phase composition and microstructure of polycrystalline and epitaxial TaN<sub>x</sub> layers grown on oxidized Si (001) and MgO (001) by reactive magnetron sputter deposition. *Thin Solid Films* **2002**, *402*, 172–182. [[CrossRef](#)]
32. Toth, L. *Transition Metal Carbides and Nitrides*; Academic Press: New York, NY, USA, 1971; pp. 150–160.
33. Kuo, Y. Reactive ion etching of sputter deposited tantalum oxide and its etch selectivity to tantalum. *J. Electrochem. Soc.* **1992**, *139*, 579. [[CrossRef](#)]
34. Sasaki, K.; Noya, A.; Umezawa, T. Stoichiometry of Ta–N Film and Its Application for Diffusion Barrier in the Al<sub>3</sub>Ta/Ta–N/Si Contact System. *Jpn. J. Appl. Phys.* **1990**, *29*, 1043. [[CrossRef](#)]

35. Lim, Y.L.; Chaudhri, M.M. The influence of grain size on the indentation hardness of high-purity copper and aluminium. *Philos. Mag. A* **2002**, *82*, 2071–2080. [[CrossRef](#)]
36. Musil, J. Hard nanocomposite coatings: Thermal stability, oxidation resistance and toughness. *Surf. Coat. Technol.* **2012**, *207*, 50–65. [[CrossRef](#)]
37. Zhang, M.; Jiang, J.; Houska, J.; Kohout, J.; Vlcek, J.; Meletis, E.I. A study of the microstructure evolution of hard Zr–B–C–N films by high-resolution transmission electron microscopy. *Acta Mater.* **2014**, *77*, 212–222. [[CrossRef](#)]
38. Leyland, A.; Matthews, A. On the significance of the  $H/E$  ratio in wear control: A nanocomposite coating approach to optimised tribological behaviour. *Wear* **2000**, *246*, 1–11. [[CrossRef](#)]
39. Yan, X.; Yin, J.; Cheng, X.; Liu, J. Tribological properties of Ta–C–N and Ta–N thin films. *Mater. Sci. Eng. Technol.* **2013**, *44*, 50–65. [[CrossRef](#)]



© 2017 by the authors. Licensee MDPI, Basel, Switzerland. This article is an open access article distributed under the terms and conditions of the Creative Commons Attribution (CC BY) license (<http://creativecommons.org/licenses/by/4.0/>).